



Fine Structure of a Solar Type II Radio Burst Observed by LOFAR

Jasmina Magdalenic¹, Christophe Marqué¹, Richard A. Fallows², Gottfried Mann³, Christian Vocks³, Pietro Zucca²,
Bartosz P. Dabrowski⁴, Andrzej Krankowski⁴, and Valentin Melnik⁵

¹ Solar-Terrestrial Centre of Excellence—SIDC, Royal Observatory of Belgium, 3 Avenue Circulaire, B-1180 Uccle, Belgium; jasmina.magdalenic@sidc.be

² ASTRON—The Netherlands Institute for Radio Astronomy, Oude Hoogeveensedijk 4, 7991 PD Dwingeloo, The Netherlands

³ Leibniz-Institut für Astrophysik Potsdam (AIP), An der Sternwarte 16, D-14482 Potsdam, Germany

⁴ Space Radio-Diagnostics Research Centre, University of Warmia and Mazury in Olsztyn, Poland

⁵ Institute of Radio Astronomy, National Academy of Sciences of Ukraine, Kharkov, Ukraine

Received 2020 February 17; revised 2020 June 5; accepted 2020 June 9; published 2020 July 1

Abstract

Shock waves in the solar corona are closely associated with coronal mass ejections and flares. The longest-known and frequently studied signatures of coronal shock waves are metric type II radio bursts, which provide information on the shock driver and ambient plasma conditions. We report on outstanding high frequency/time resolution LOW Frequency ARray (LOFAR) observations of a metric type II radio burst. The LOFAR observations show a strong fragmentation of the type II emission, in both the frequency and time domains, during the whole duration of the event. A very unusual splitting of an already-split type II band, which we call the band-split of the band-split, was observed for the first time. The richness of fine structure, observed in both the fundamental and harmonic bands of the type II emission, is unprecedented. Fine structures, morphologically similar to those seen superposed on a type IV continuum, were observed for the first time within a type II burst. We classify the fine structures into three categories: simple narrowband, broadband, and complex fine structures, and discuss their properties. LOFAR observations of fragmented shock-associated radio emission have the potential of bringing new insight into the physics of coronal shock waves, and also new challenges for the theory of electron acceleration by shocks.

Unified Astronomy Thesaurus concepts: [Solar coronal mass ejection shocks \(1997\)](#); [Solar physics \(1476\)](#); [Solar electromagnetic emission \(1490\)](#); [Solar coronal waves \(1995\)](#); [Active solar corona \(1988\)](#); [Solar radio emission \(1522\)](#)

1. Introduction

Solar eruptive processes, such as flares and coronal mass ejections (CMEs) are associated with electromagnetic emission covering a wide spectral range. CME-driven shock waves accelerate nonthermal electrons that can generate radio bursts. These so-called type II bursts (e.g., Wild 1950; Nelson & Melrose 1985; Vršnak & Cliver 2008; Mann 2006; Magdalenic et al. 2010; Mann et al. 2018) are observed in dynamic spectra as slowly drifting emission bands. The present explanation of type II emission involves shock-accelerated electrons generating Langmuir waves at the fundamental electron plasma frequency and/or its harmonic (hereafter F and H band). Sometimes type II bursts show fine structures (FSs), e.g., the F and H bands are split into two parallel lanes of similar frequency drifts and intensity behavior, a so-called band-split (e.g., Smerd et al. 1974; Smerd et al. 1975; Holman & Pesses 1983; Nelson & Melrose 1985; Vršnak et al. 2001). The main emission component can be accompanied by fast drifting features, so-called herringbones (Roberts 1959). So far only occasional works were devoted to type II FSs (e.g., Vršnak et al. 2001, 2002; Carley et al. 2015; Dorovskyy et al. 2015). Although fragmentation of the type II emission was occasionally reported, it was observed either exclusively in the decameter range, at single frequencies or only at the beginning of the type II burst (e.g., Chernov et al. 1975, 2007; Urbarz et al. 1977; Zlobec & Thejappa 1987; Armatas et al. 2019). Recently, a new generation of radio telescopes has been developed, in the form of numerous small antennas with a large collective area and high sensitivity, such as, e.g., the LOW Frequency ARray (LOFAR; van Haarlem et al. 2013). LOFAR

already significantly improved the quality of solar radio observations, in terms of frequency coverage and frequency/time resolution, and brought new insight into the physics of metric and decametric radio emission and associated eruptive phenomena (e.g., Morosan et al. 2015).

In this Letter we present high-resolution LOFAR observations of a strongly fragmented type II burst from 2014 August 25. In Section 2, the CME/flare event and the associated radio event are presented. Section 3 is devoted to description of the type II FSs and their characteristics, and Section 4 to summary and conclusions.

2. Solar Eruptive Event and Associated Radio Emission on 2014 August 25

2.1. Eruptive Event

The Geostationary Operational Environmental Satellite (GOES) observations show an M2.0 flare with two maxima (14:54 and 15:10 UT). The flare originated from NOAA AR 2146 (N09° W47°) and was associated with the rise of a coronal loop system, two brightenings observed by the Atmospheric Imaging Assembly (AIA) on board the Solar Dynamics Observatory (SDO; Lemen et al. 2012), a coronal dimming, and an EIT wave (Zhukov 2011; Liu & Ofman 2014) propagating westward of the source region. The associated full halo CME had a plane-of-sky speed of 500 km s⁻¹ and was first seen by the Large Angle and Spectrometric CORonagraph instruments (LASCO; Brueckner et al. 1995) on board the Solar and Heliospheric Observatory (SOHO; Domingo et al. 1995) at 15:24 UT.

2.2. Radio Event

The radio event was observed using both the Low Band Antennas (LBAs; 10–90 MHz) and High Band Antennas (HBAs; 110–240 MHz) of LOFAR. It is the first instrument to make simultaneous dynamic spectra and imaging observations in the frequency range connecting the corona and interplanetary space. Since LOFAR frequencies partially overlap with the ones of the Nançay radioheliograph (NRH; 150–450 MHz; Kerdraon & Delouis 1997), we performed for the first time a comparison of imaging observations for a type II burst.

The frequency/time resolution of the dynamic spectra recorded by LOFAR was 12.3 kHz and 0.01 s, respectively, and were obtained using both the LBA and HBA bands. Imaging observations were taken in the HBA band only. The dynamic spectra (Figure 1(a)) show a textbook example of radio emission associated with a CME/flare event. It consists of type III bursts indicating the impulsive phase of the flare, followed by a type II burst, and a broadband type IV continuum. The majority of the intense type III bursts (14:57–15:03 UT) are structured, showing fragmentation similar to type II emission. The type II burst consists of a short-high-frequency part observed by HBA, and an intense, strongly fragmented, part observed by LBA. The LBA type II shows well-defined *F* and *H* bands. Some of the type III bursts were also observed by STEREO-B/Waves (Kaiser 2005; Bougeret et al. 2008), but the type II burst was observed only by WIND/Waves (Bougeret et al. 1995). The metric type II emission (flux intensity of ≈ 1000 sfu) is weakening in intensity and decreasing in bandwidth while continuing into the decameter range (observed down to 4 MHz).

3. Characteristics of the Type II Radio Burst

The main characteristic of the type II burst is the strong fragmentation of the radio emission during the whole type II burst, observed in both the *F* and *H* bands. The LOFAR spectrum shown with time resolution decreased to 0.25 s (Figure 1), mimics low-resolution observations, and shows a typical type II burst. However, the full resolution dynamic spectrum (Figure 2) shows strong structuring of the type II emission, in particular at the beginning and in the middle of the event. Toward the end of the burst a gradual transition from highly structured to smoother emission is observed, concurrent with a strong decrease in intensity and bandwidth (simultaneous for both bands). A change in type II fragmentation during the course of an event observed at a single frequency was reported by Zlobec & Thejappa (1987).

The HBA type II (Figure 1(b)) appears detached from the LBA type II and shows only one band with a clear band-split. The most frequently considered interpretation of the band-split is emission from upstream and downstream shock regions (Smerd et al. 1974; Smerd et al. 1975; see Vršnak et al. 2001 and references therein for a detailed discussion on this and other possible explanations). Assuming this hypothesis for the HBA type II band-split and a 3.5-fold Saito density model (Saito 1970) we obtained an ambient Alfvén velocity of 600 km s^{-1} . We note that this density model is considered as appropriate for C-class and low M-class flare events (Magdalenic et al. 2008, 2010, 2012).

The type II emission seen in HBA is probably harmonic as it is more difficult for fundamental plasma emission to escape the low corona. The *F* band should then be observed between 90

and 70 MHz, which is within the LOFAR LBA band, but a hard filter in the receiver strongly reduces the signal above ≈ 78 MHz. However, a back-extrapolation from the LBA type II fits well to the HBA type II, indicating that they are both signatures of the same shock wave (Figure 1(c)). Using the type II drift rate and the often used 3.5-fold Saito density model we obtained a shock wave velocity of $\approx 800 \text{ km s}^{-1}$.

Figure 1(d) shows the first comparison of simultaneous LOFAR and NRH images of a type II burst. As expected the sources are copatial, but of slightly different shapes, reflecting differences in instrumentation and data processing. Figures 1(e) and (f) show simultaneous positions of the HBA type II band-split pairs (times marked in Figure 1(b) with dashed lines). A small but systematic shift of the source positions is observed. Since the shift is noticeably larger for the high-frequency pair than for the low-frequency pair (Figures 1(f) and (e)), we believe that the shift is not induced by scattering effects (Chrysaphi et al. 2018), but that it reflects the shock wave geometry.

While the HBA type II shows a simple band-split, the situation is more complex for the LBA type II. After the change in the type II drift at 15:13 UT (better observed for the *F* band), a very peculiar splitting of the already-split *H* band was observed (Figure 2(b)). To our knowledge this is the first report of a *band-split of the band-split* of the type II burst. The split is about 8 MHz wide and lasts 2 minutes. Preliminary analysis of the associated EIT wave indicates deceleration of the wave approximately at the time of the band-split of the band-split. The constant split of the bands suggests that, regardless of the cause, similar plasma conditions near the shock front had to be maintained for about 2 minutes, during which four lanes are observed.

3.1. Classification of Type II Fine Structures

The type II consists of a broad variety of FSs morphologically similar to super-short structures (SSSs) within type IV continua (Magdalenic et al. 2006), so we used similar classification criteria. We distinguish three main categories of FSs: (1) simple narrowband, (2) simple broadband, and (3) complex FSs (Table 1). For easier identification, a one-to-one schematic presentation of groups of FSs is shown in Figures 3(e) and 4(e).

3.1.1. Simple Narrowband FSs

The frequent simple narrowband FS are (1) flag-like, (2) dot-like, (3) sail-like, (4) hair-like, and (5) spike-like bursts (Figure 3). Due to particular morphology of narrowband FSs, the derived durations are variable and strongly depend on the frequency at which they are estimated. The frequency extent, i.e., bandwidth of narrowband FSs is, for a majority of bursts, below 1 MHz (Table 1).

Flag-like bursts (Figure 3, black arrows) have symmetric frequency profiles and strongly asymmetric time profiles, with a steep profile in the rising phase of the burst. When they appear in groups, their characteristics are more homogeneous than for isolated bursts. They are observed mostly in the beginning and in the middle part of the type II.

Sail-like bursts (Figure 3, blue arrows) have a triangular spectral shape, symmetrical frequency profile, and asymmetric time profiles. They are mostly observed in the beginning of the

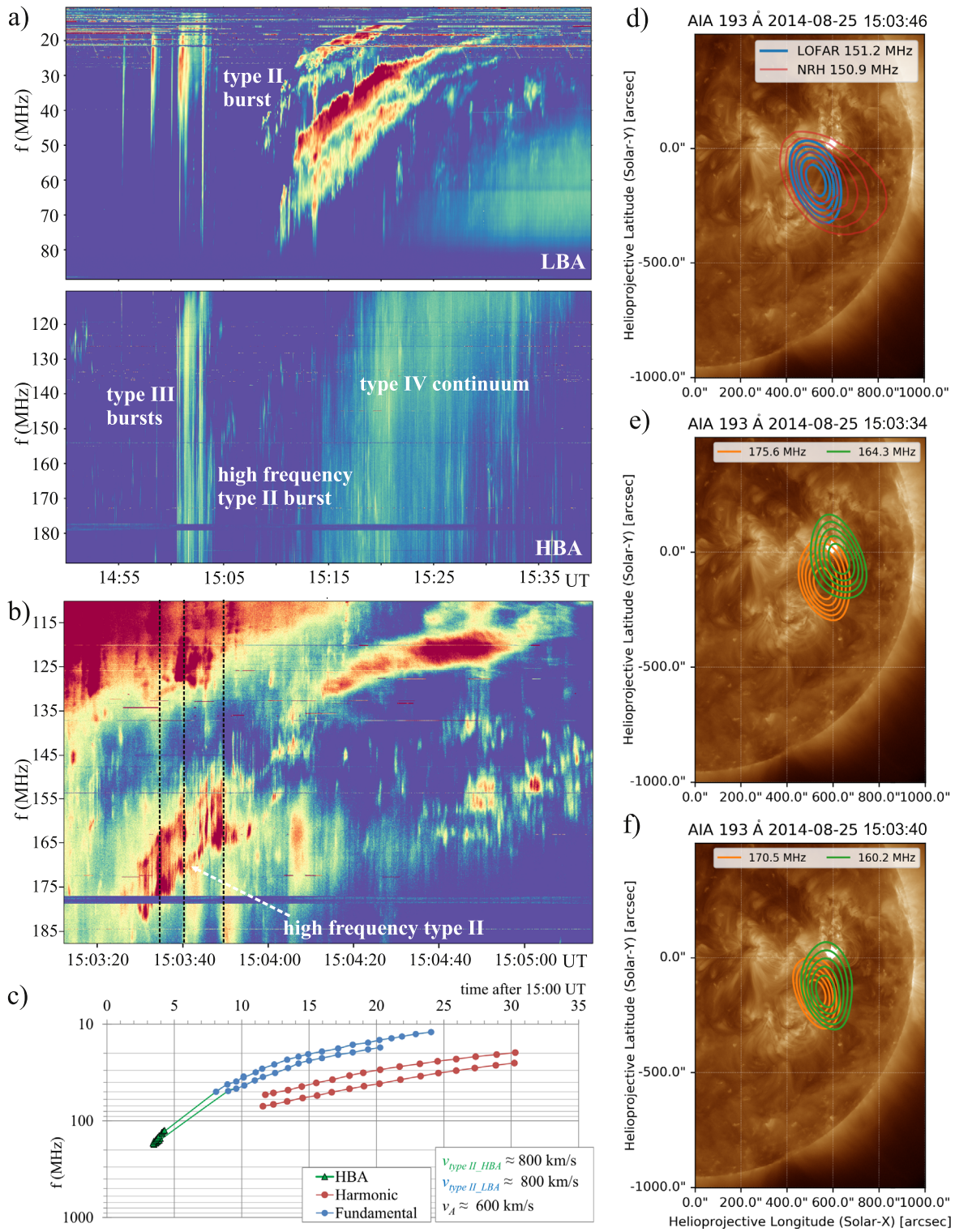


Figure 1. (a) Dynamic spectrum with reduced time/frequency resolutions of the radio event on 2014 August 25. (b) Detail of the high-frequency component of the type II burst in the HBA observation. (c) Kinematics of the type II radio burst. (d) Comparison of LOFAR and NRH images of the high-frequency type II sources. Radio sources are overlaid using images taken the closest together in time 193 Å. (e) and (f) Images of two pairs of simultaneous sources of the high-frequency type II band-split.

type II burst and are narrowband FSs with the largest bandwidth (≤ 1 to ≈ 1.5 MHz).

Dot-like bursts (Figure 3, white arrows) appear in a broad range of intensities and have symmetric time and frequency profiles. It is difficult to isolate them from other narrowband

FSs as they often gradually transform to sail-like or flag-like bursts. They mostly appear in stochastic groups, and sometimes they form different types of complex bursts, e.g., inverse type IIIb-like (Figure 4(d)). They are observed during the whole type II burst.

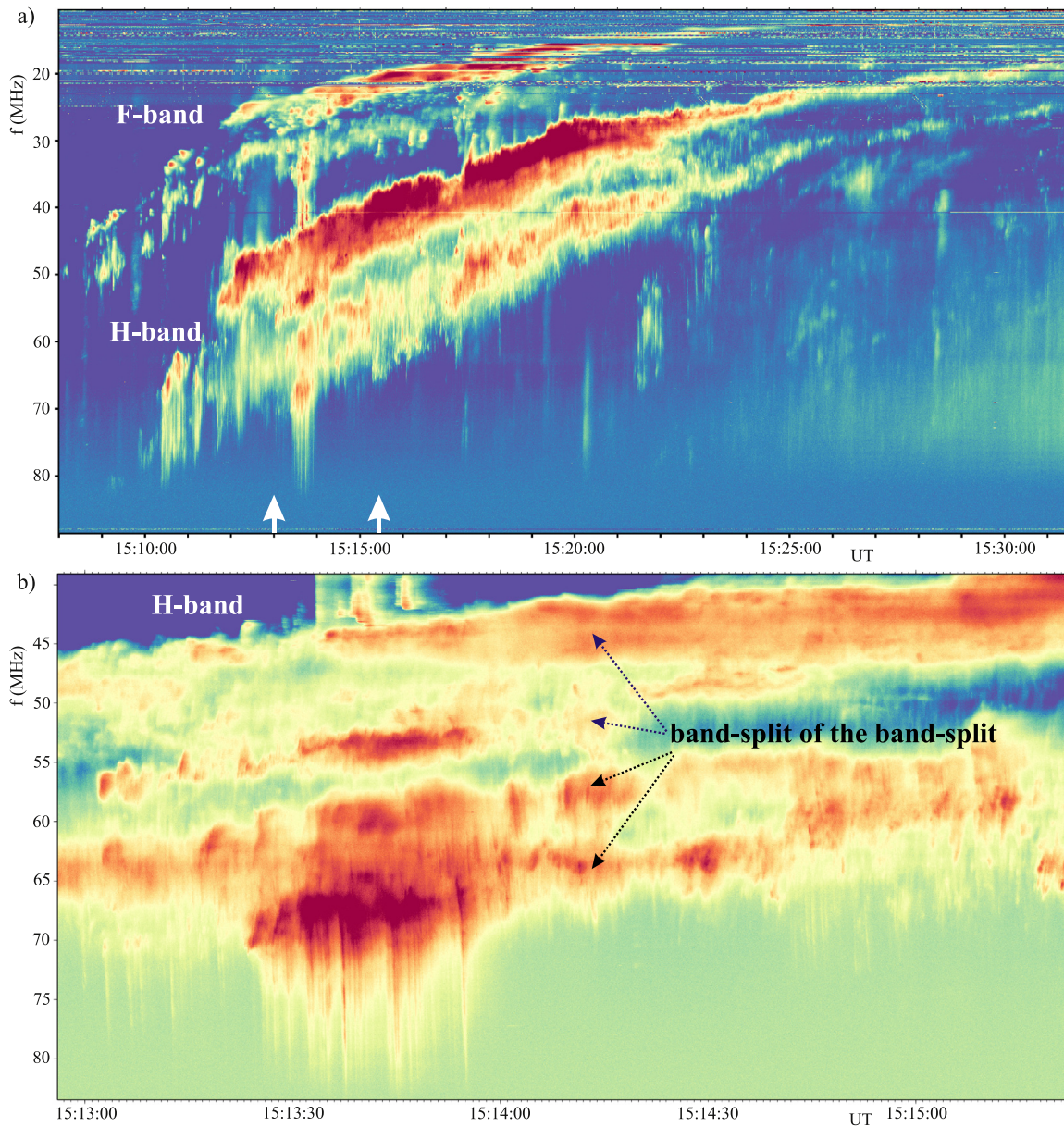


Figure 2. Dynamic spectrum observed by LOFAR showing (a) the type II burst observed at full resolution and (b) the band-split of the band-split. The white arrows at the bottom of dynamic spectrum in panel (a) indicate the time interval plotted in panel (b).

Table 1
Main Characteristics of Different Classes of Type II FSs

| Name | Spectral Category | Full Duration $\Delta t(s)$ | Δf (MHz) | $ \Delta f / \Delta t $ (MHz s ⁻¹) | Comment |
|------------------------|-------------------|-----------------------------|------------------|---|---------------------------------|
| flag-like | narrowband | 1.07–11.53 | 0.09–1.00 | ... | very diverse duration |
| sail-like | narrowband | 0.44–1.06 | 0.71–1.62 | 1.40–3.50 | rather rare |
| dot-like | narrowband | 0.15–1.60 | 0.16–0.88 | ... | most frequent |
| hair-like | narrowband | 0.58–2.07 | 0.03–0.09 | ... | narrowest bandwidths |
| spike-like | narrowband | 0.09–0.39 | 0.30–0.96 | ∞ | numerous toward the type II end |
| herringbones | broadband | variable | up to 20 | ≈ 25 | diverse bandwidths |
| pulses | broadband | 0.01–0.10 | ≈ 10 | ... | diverse drift orientations |
| complex herringbones | complex | ... | up to 20 | ≈ 0.03 (before the brake) ≈ 0.13 (after the brake) | reverse drifts only |
| inverse type IIIb like | complex | 0.20–0.50 | 5–10 | 5–23 | reverse drifts only |
| complex J-bursts | complex | ... | ≈ 2 | ... | diverse frequency extents |

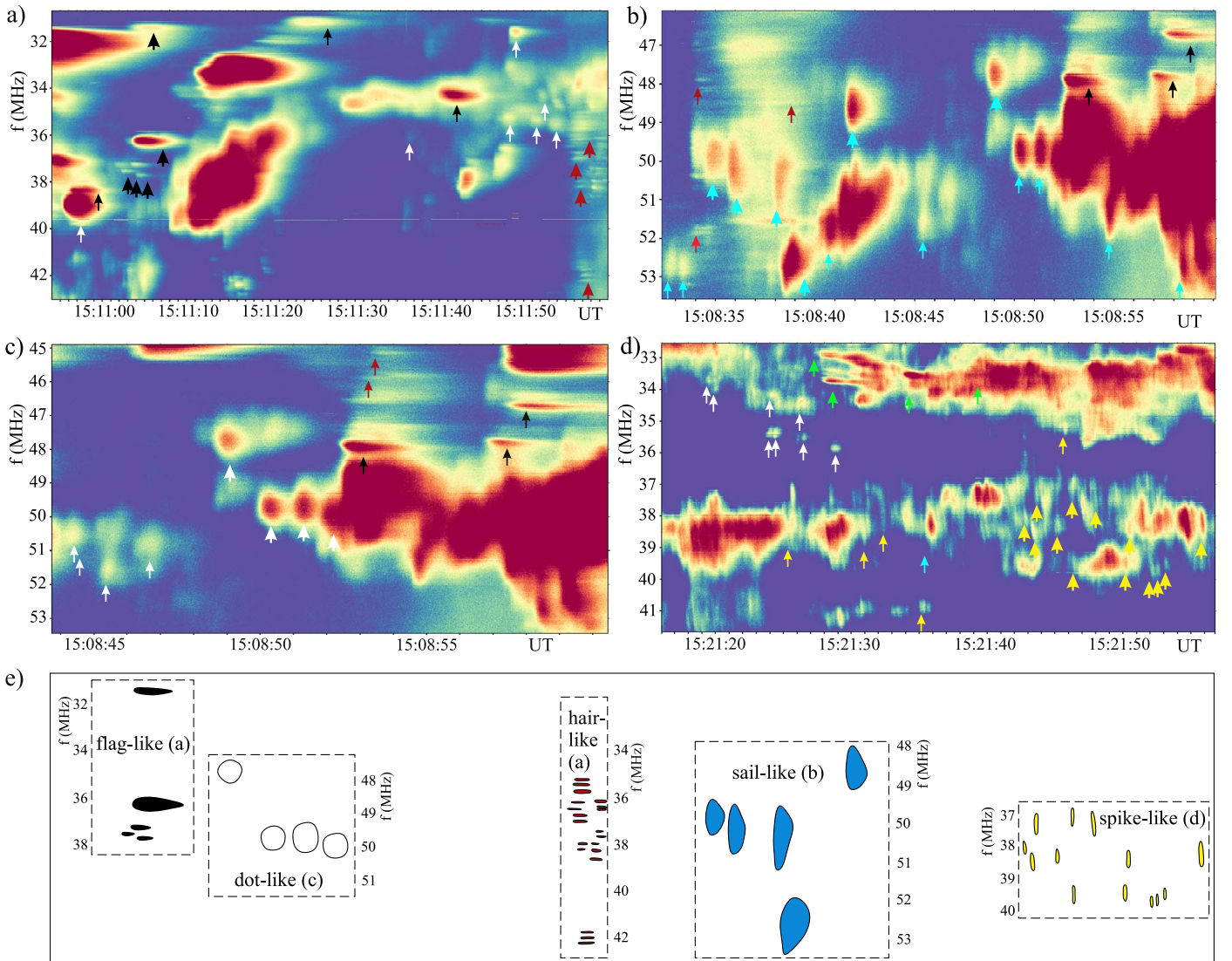


Figure 3. Panels (a)–(d) show LOFAR dynamic spectra of different narrowband FSs in the type II burst. In all dynamic spectra flag-like bursts are denoted with thick black arrows, dot-like with white, sail-like with blue, hair-like with red, and spike-like with yellow arrows. (e) One-to-one schematic presentation of selected groups of FSs presented in panels (a)–(d).

Hair-like bursts (Figure 3, red arrows) are the most numerous FSs and have the narrowest frequency bandwidth (typically 0.03–0.09 MHz); some of them may not be fully resolved. Their intensity is lower than the other FSs, and they are mostly observed close to the edge of the type II emission. Hair-like bursts can appear randomly, as well as in defined pairs, or in a vertical envelope. For bursts within an envelope, duration, frequency bandwidth, and even the frequency separation between two bursts are well defined, and do not show systematic changes in the course of time. When hair-like bursts are observed in nonorganized groups, their characteristics vary from burst to burst. Although for the majority of hair-like bursts the drift is approximately zero, bursts with positive and negative drifts are sometimes observed.

Spike-like bursts (Figure 3, yellow arrows) are also very frequent FSs. At the beginning and in the middle of the type II burst they are more rare and often superposed on other types of FSs. Toward the end of the type II burst they become more dominant. Their characteristics are similar to those of classical spikes (e.g., Bouratzis et al. 2016) superposed on type IV continua later in the event (Figure 1).

3.1.2. Simple Broadband FSs

Simple broadband FSs have a bandwidth of a few to 10 MHz, comparable to the bandwidth of the type II burst. We distinguish two main classes: (1) herringbones and (2) pulses (Figure 4 and Table 1).

The *herringbones* are observed mostly in the middle of the type II burst, and are not dominant FSs, which is consistent with previous studies (e.g., Slottje 1972; Mann & Klassen 2005; Carley et al. 2015). They drift from the high-frequency edge of both the *F* and *H* bands, but the low-frequency parts of both bands show a sharply defined emission edge with occasional short, J-like, bursts streaming toward low frequencies (Figure 2(b)). Their drift of $\approx 25 \text{ MHz s}^{-1}$ is about twice that reported by Carley et al. (2015). The majority of herringbones have reverse drifts, while bursts with a forward drift are rare. We did not observe pairs of herringbones simultaneously having positive and negative drifts, indicating that beams generating the herringbones are not bidirectional.

Pulses are instantaneous bursts that typically appear in groups (Figure 4(a)). Their bandwidth is either well defined for

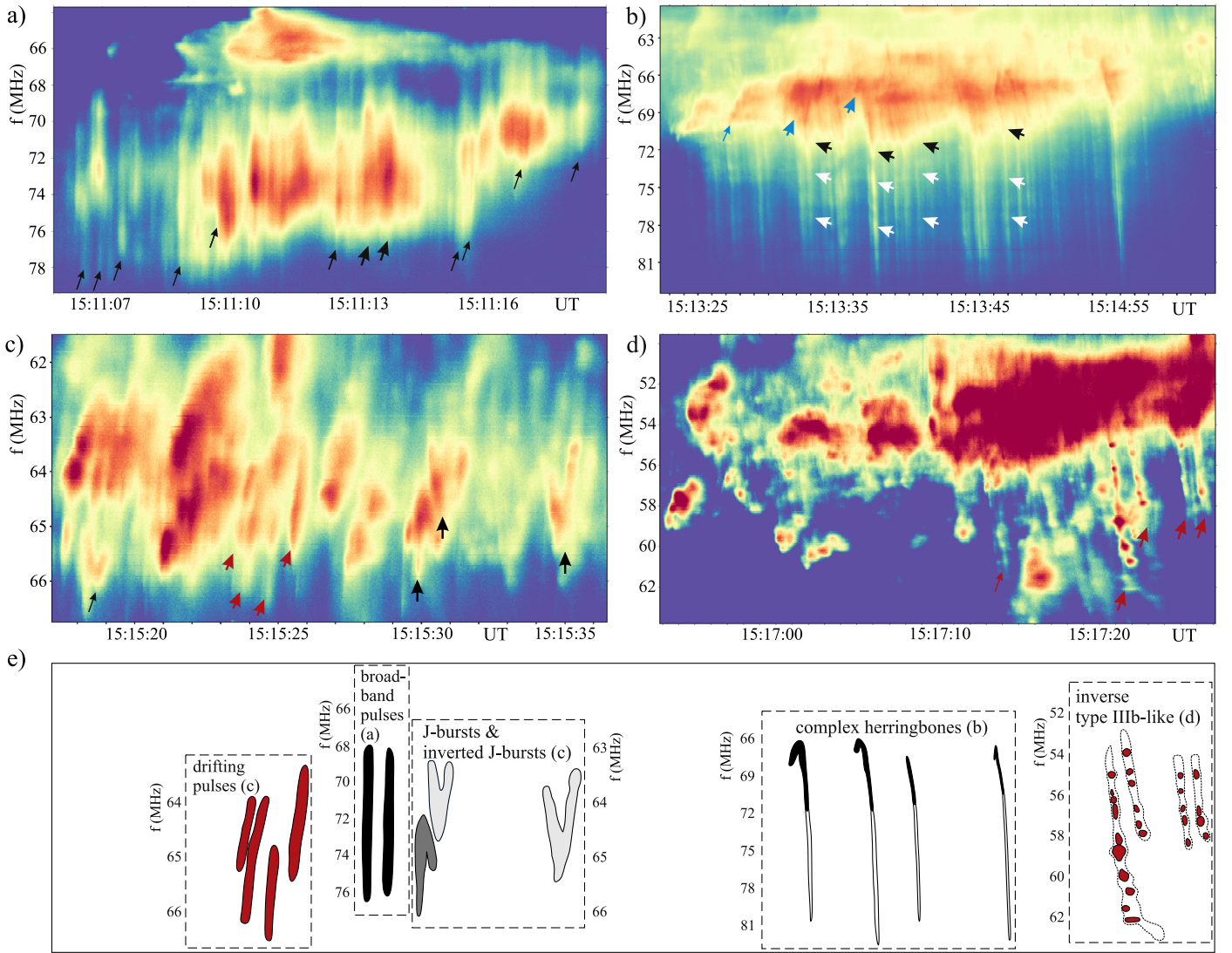


Figure 4. LOFAR dynamic spectra showing (a) broadband pulses, (b) complex herringbones (blue arrows denote the J part of the burst, black arrows denote “the break” in the burst indicating a change in the frequency drift), (c) J-bursts and drifting pulses (marked with black and red arrows, respectively), (d) inverse type IIIb-like bursts composed of narrowband dot-like FSs in a faint drifting envelope, and (e) a one-to-one schematic presentation of selected broadband FSs shown in panels (a)–(d).

an individual group (≈ 12 MHz), or gradually changes within the group. The time profiles are similar along the burst, and most pulses within the group show periodicity, such as short-duration pulsations (see the review by Chernov 2011) and SSS pulses (Magdalenic et al. 2006). Sporadically, drifting pulses of both positive and negative drift are also observed (Figure 4(c)).

3.1.3. Complex FSs

LOFAR observations reveal that both narrowband and broadband FSs frequently constitute complex bursts. The most prominent complex FSs are (1) complex herringbones, (2) inverse type IIIb-like bursts, and (3) complex J-bursts. The characteristics of narrowband and broadband FSs observed within the complex bursts are similar to those of isolated bursts. Further, complex herringbones and inverse type IIIb-like bursts appear only with reverse drifts.

Some of the FSs with a herringbone-like appearance are actually complex bursts. The largest group of *complex herringbones* (Figure 4(b)) shows an inverted J-like shape in

the high-frequency part and “break” in the frequency drift from 0.03 to 0.13 MHz s^{-1} (Figure 4(b), black and white arrows). Some bursts show dot-like substructures in the low-frequency part, while substructures in the high-frequency part are poorly resolved (Figure 4(b)). We note that Dorovskyy et al. (2015) reported substructures of herringbones similar to hair-like FSs.

Inverse type IIIb-like FSs are composed of narrowband dot-like FSs in a faint drifting envelope (Figure 4(d)). In the majority of these complex bursts the dot-like FSs are more intense than the burst envelope. The drift rate of the inverse type IIIb-like bursts (5 – 23 MHz s^{-1}) is comparable to the drift of herringbones.

The majority of J-bursts and inverted J-bursts (Figure 4(c), black arrows) show substructures in the form of dot-like FSs and/or drifting spikes. The *complex J-bursts* have larger bandwidths than the structureless J-bursts observed mostly at the low-frequency edge of the *H* band. Together with the described FSs, more patchy and complex bursts are observed,

e.g., horizontal bursts marked with green arrows in Figure 3(d). The richness of different type II FSs suggests very dynamic plasma conditions at different spatial and temporal scales in front and behind the shock.

4. Summary and Discussion

We report for the first time on the extraordinary fragmentation of a type II radio emission, observed in high-resolution LOFAR data. We highlight the main findings of the Letter:

1. We presented strong fragmentation of type II emission, observed in both the *F* and *H* bands. The FSs were observed during the whole type II burst.
2. The most interesting type II property reported for the first time is what we call a band-split of the band-split (Figure 2). During 2 minutes the *H* band is split into four parallel lanes with a stable frequency separation (≈ 8 MHz).
3. The fragmented type II shows a variety of FSs that we classified based on their morphological characteristics and in accordance with the classification of SSSs (Magdalenic et al. 2006). We distinguish three main classes: narrowband, broadband, and complex FSs. Each class comprises a few types of FSs.
4. One of the most peculiar FSs are hair-like FSs (Figure 3). These are the bursts with the narrowest frequency bandwidth (0.03–0.09 MHz) reported so far in the metric range, close to the LOFAR resolution (0.0123 MHz). Hair-like FSs sometimes constitute complex bursts, where even narrower bandwidths were observed, but poorly resolved.

We note that the CME/flare event associated with the shock wave generating the fragmented type II burst showed no particularity with respect to the flare magnitude or the CME/shock speed. The radio event was also typical: type III bursts associated with the impulsive phase of the flare were followed by a type II burst and type IV continuum. However, the high-resolution LOFAR observations show strong fragmentation of the radio emission. Fragmentation of type II bursts has occasionally been reported before, but only at a single frequency (Zlobec & Thejappa 1987), in a very limited frequency range (Chernov et al. 2007; Dorovskyy et al. 2015), or at lower frequency or time resolution (Armatas et al. 2019; 0.01 s and 1 MHz). This is the first report of type II fragmentation on such a fine frequency/timescale, observed during the whole duration of the type II burst, and for both the *F* and *H* bands. The fragmentation was stronger on the frequency scale than on the temporal scale. Fragmentation of the radio emission might be a frequent property of type II bursts and possibly also other types of bursts. The high-resolution LOFAR observations enabled detection of FSs that would not be visible in lower-resolution observations. The URAN-2 radio telescope (Brazhenko et al. 2005) observed the same type II burst, with a higher frequency and lower temporal resolution than LOFAR (4 kHz and 0.1 s, respectively), over a limited frequency band (12–32 MHz). However, the LOFAR observations show more fragmented type II emission than URAN-2 (V. Melnik 2020, private communication), possibly due to a higher temporal resolution.

The first step toward understanding this fragmentation is to confirm that this is a general characteristic of type II bursts, and

not particular to this event. For that purpose the same LOFAR observing mode should be used for more type II observations.

The reasons for fragmentation of the shock-associated radio emission may be very diverse. One of the possibilities is that the FSs are generated when the shock wave propagates in a strongly inhomogeneous and turbulent plasma, with various structures of density and magnetic field (see, e.g., Andreopoulos et al. 2000). The extent of the emission patches within the type II burst is defined by the shock crossing time of one turbulence eddy. The intensity of the FS emission is then related to the small-scale turbulence that increases the conversion efficiency of plasma waves into electromagnetic waves (e.g., Zaitsev & Fomichev 1973). If the shock propagates across very structured magnetic fields, e.g., near active regions, the presence of numerous, small, collapsing trap configurations created by the wavy shock front and magnetic field lines is also possible (Magdalenic et al. 2002; Vandas & Karlický 2011). These scenarios could also explain the decrease in fragmentation of the type II emission at lower frequencies (detected by visual inspection), as the shock reaches the less structured upper corona.

Theoretical explanations of type II FSs need to account for identical types of FSs observed in both the *F* and *H* bands, groups of FSs with similar characteristics, transition of one FS type into another, and complex FSs composed of narrowband and/or broadband FSs. The presented observations bring new insight into the morphological structure of the shock-associated radio emission and point to the need to revisit the mechanisms responsible for the generation of shock-associated radio emission and its fine structure.

J.M. is dedicating this Letter to the memory of her teacher and friend Dr Paolo Zlobec, a renowned solar radio physicist who made a large contribution to the study of radio fine structures. J.M. acknowledges funding by the BRAIN-be (Belgian Research Action through Interdisciplinary Networks) project CCSOM (Constraining CMEs and Shocks by Observations and Modeling throughout the inner heliosphere). This Letter is based on data obtained with the International LOFAR Telescope (ILT) under project code LC2_033. LOFAR (van Haarlem et al. 2013) is the Low Frequency Array designed and constructed by ASTRON. It has observing, data processing, and data storage facilities in several countries, that are owned by various parties (each with their own funding sources), and that are collectively operated by the ILT foundation under a joint scientific policy. The ILT resources have benefited from the following recent major funding sources: CNRS-INSU, Observatoire de Paris and Université d'Orléans, France; BMBF, MIWF-NRW, MPG, Germany; Science Foundation Ireland (SFI), Department of Business, Enterprise and Innovation (DBEI), Ireland; NWO, The Netherlands; The Science and Technology Facilities Council, UK; Ministry of Science and Higher Education, Poland.

ORCID iDs

Jasmina Magdalenic  <https://orcid.org/0000-0003-1169-3722>

Richard A. Fallows  <https://orcid.org/0000-0002-5186-8040>

Christian Vocks  <https://orcid.org/0000-0001-8583-8619>

Pietro Zucca  <https://orcid.org/0000-0002-6760-797X>

Bartosz P. Dabrowski  <https://orcid.org/0000-0002-4705-7798>

Andrzej Krankowski  <https://orcid.org/0000-0003-2812-6222>

Valentin Melnik  <https://orcid.org/0000-0001-9239-6548>

References

- Andreopoulos, Y., Agui, J. H., & Briassulis, G. 2000, *AnRFM*, **32**, 309
- Armatas, S., Bouratzis, C., Hillaris, A., et al. 2019, *A&A*, **624**, A76
- Bougeret, J. L., Goetz, K., Kaiser, M. L., et al. 2008, *SSRv*, **136**, 487
- Bougeret, J.-L., Kaiser, M. L., Kellogg, P. J., et al. 1995, *SSRv*, **71**, 231
- Bouratzis, C., Hillaris, A., Alistandrakis, C. E., et al. 2016, *A&A*, **586**, A29
- Brazhenko, A. I., Bulatsen, V. G., Vashchishin, R. V., et al. 2005, *KFNTS*, **5**, 43
- Brueckner, G. E., Howard, R. A., Koomen, M. J., et al. 1995, *SoPh*, **162**, 357
- Carley, E. P., Reid, H., Vilmer, N., & Gallagher, P. T. 2015, *A&A*, **581**, A100
- Chernov, G. 2011, *Fine Structure of Solar Radio Bursts*, *Astrophysics and Space Science Library*, Vol. 375 (Berlin: Springer)
- Chernov, G. P., Korolev, O. S., & Markeev, A. K. 1975, *SoPh*, **44**, 435
- Chernov, G. P., Stanislavsky, A. A., Konvalenko, A. A., et al. 2007, *AstL*, **33**, 192
- Chrysaphi, N., Kontar, E. P., Holman, G. D., & Temmer, M. 2018, *ApJ*, **868**, 79
- Domingo, V., Fleck, B., & Poland, A. I. 1995, *SoPh*, **162**, 1
- Dorovsky, V. V., Melnik, V. N., Konvalenko, A. A., et al. 2015, *SoPh*, **290**, 2031
- Holman, G. D., & Pesses, M. E. 1983, *ApJ*, **267**, 837
- Kaiser, M. L. 2005, *AdSpR*, **36**, 1483
- Kerdraon, A., & Delouis, J.-M. 1997, in *Coronal Physics from Radio and Space Observations*, Vol. 483, ed. G. Trotter (Berlin: Springer), 192
- Lemen, J. R., Title, A. M., Akin, D. J., et al. 2012, *SoPh*, **275**, 17
- Liu, W., & Ofman, L. 2014, *SoPh*, **289**, 3233
- Magdalenic, J., Marqué, C., Zhukov, A. N., et al. 2010, *ApJ*, **718**, 266
- Magdalenic, J., Marqué, C., Zhukov, A. N., et al. 2012, *ApJ*, **746**, 152
- Magdalenic, J., Vršnak, B., & Aurass, H. 2002, in *ESA SP-506, Solar Variability: From Core to Outer Frontiers*, ed. A. Wilson (Noordwijk: ESA), 335
- Magdalenic, J., Vršnak, B., Pohjolainen, S., et al. 2008, *SoPh*, **253**, 305
- Magdalenic, J., Vršnak, B., Zlobec, P., Hillaris, A., & Messerotti, M. 2006, *ApJL*, **642**, L77
- Mann, G. 2006, *GMS*, **165**, 221
- Mann, G., & Klassen, A. 2005, *A&A*, **441**, 319
- Mann, G., Melnik, V. N., Rucker, H. O., Konvalenko, A. A., & Brazhenko, A. I. 2018, *A&A*, **609**, A41
- Morosan, D. E., Gallagher, P. T., Zucca, P., et al. 2015, *A&A*, **580**, A65
- Nelson, G. J., & Melrose, D. B. 1985, in *Solar Radiophysics: Studies of Emission from the Sun at Metre Wavelengths*, ed. D. J. McLean & N. R. Labrum (Cambridge: Cambridge Univ. Press), 333
- Roberts, J. A. 1959, *AuJPh*, **12**, 327
- Saito, K. 1970, *AnTok*, **12**, 51
- Slottje, C. 1972, *SoPh*, **25**, 210
- Smerd, S. F., Sheridan, K. V., & Stewart, R. T. 1974, in *IAU Symp. 57, Coronal Disturbances*, ed. G. A. Newkirk (Dordrecht: Reidel), 389
- Smerd, S. F., Sheridan, K. V., & Stewart, R. T. 1975, *ApL*, **16**, 23
- Urbarz, H. W., Fomichev, V. V., & Chertok, I. M. 1977, *SvA*, **21**, 77
- Vandas, M., & Karlický, M. 2011, *A&A*, **531**, A55
- van Haarlem, M. P., Wise, M. W., Gunst, A. W., et al. 2013, *A&A*, **556**, A2
- Vršnak, B., Aurass, H., Magdalenic, J., & Gopalswamy, N. 2001, *A&A*, **377**, 321
- Vršnak, B., & Cliver, E. W. 2008, *SoPh*, **253**, 215
- Vršnak, B., Magdalenic, J., Aurass, H., & Mann, G. 2002, *A&A*, **396**, 673
- Wild, J. P. 1950, *AuSRA*, **3**, 399
- Zaitsev, V. V., & Fomichev, V. V. 1973, *SvA*, **16**, 666
- Zhukov, A. N. 2011, *JASTP*, **73**, 1096
- Zlobec, P., & Thejappa, G. 1987, *HvaOB*, **11**, 111